ACS Energy LETTERS

http://pubs.acs.org/journal/aelccp

What Structural Features Make Porous Carbons Work for Redox-Enhanced Electrochemical Capacitors? A Fundamental Investigation

Yang Zhao, Erin E. Taylor, Xudong Hu, Brian Evanko, Xiaojun Zeng, Hengbin Wang, Ryohji Ohnishi, Takaki Tsukazaki, Jian-Feng Li,* Nicholas P. Stadie, Seung Joon Yoo,* Galen D. Stucky, and Shannon W. Boettcher*

Cite This: *ACS Energy Lett.* 2021, 6, 854−861 **Read Online**

ABSTRACT: **The addition of redox-active molecules into electrochemical-capacitor electrolytes provides increased specific energy density. Here we illustrate the underlying operational mechanisms and design principles for carbons with hierarchical pore sizes in the micropore (0.6−2 nm) to mesopore (2−3 nm, 5−30 nm) range as electrode materials in redox-enhanced electrochemical capacitors. When using iodide as a model redox additive, we discover that the redox capacity is correlated to the pore volume of the carbon electrodes when void space is included. The fastest rates are typically observed with pore-sizes >1 nm, while slow self-discharge requires pores <1 nm. When used without an ion-selective-membrane separator, the delivered capacity correlated with the quantity of redox species held within the carbon. A commercial microporous carbon, MSC30, with substantial hierarchy in pore size, including small <0.8 nm pores and larger 1.1−3 nm pores, showed the best overall performance, illustrating key design principles.**

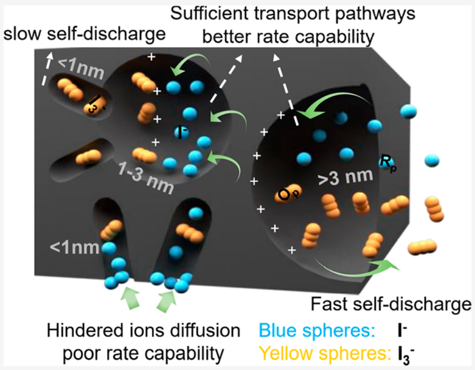

Electrochemical energy storage is important as the world decarbonizes and electrifies. Devices such as supercapacitors or electrochemical capacitors (ECs) can deliver high power and exceptional cycle life (often $>10^6$ cycles) compared to secondary batteries but have low specific energy. A "redox-enhanced" strategy utilizing reversible redox reactions in the electrolyte to add Faradaic charge storage increases the energy density of ECs. These features could make them useful in the growing automotive market.[1−5] The performance of redox-enhanced ECs (redox ECs) is limited in part, however, by self discharge due to the uncontrolled and unwanted diffusion of the charged redox species, resulting in charge losses.[6]

Despite improvements in the electrolyte formulations and expanded fundamental understanding of electrolyte processes in redox ECs,[7−10] a basic understanding of how the carbon electrode material's structure, which usually consists of a hierarchy of pore sizes ranging from subnanometers to many microns in the free space, affects performance is missing. For redox ECs, where diffusive transport of the soluble redox couple is critical, a network of larger pores is likely important for higher power. However, there is an expected trade-off between the pore size and the specific surface area (SSA). Smaller pores that contribute substantially to the SSA should affect self-discharge in the charged cell by adsorbing and confining the redox species (that form sparingly soluble complexes when charged in the most-successful implementations).[11] This trade-off suggests hierarchically porous structures are needed for optimal power, capacity, and self-discharge behavior.

Several studies have discussed the behavior of aqueous redox couples using porous carbon electrodes. Larger capacity was observed with a higher total surface area (1470 vs 676 m^2/g) and a larger average pore size (1.36 vs 1.06 nm) when 1 M KI was used as the electrolyte.[12] In separate work, activated

Received: November 19, 2020
Accepted: February 1, 2021
Published: February 5, 2021

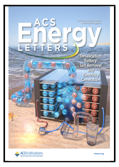

https://dx.doi.org/10.1021/acsenergylett.0c02424

carbon with larger pores (2−3 nm) was claimed to exhibit higher specific capacity when 0.08 M KI was added in 1 M H_2SO_4 electrolyte.[13] Low self-discharge rates were credited to nanopores less than 1 nm in size when using ZnI_2 redox species.[14] From these studies, however, no general guidelines regarding the roles of the different pore sizes are clear.

While several studies have illustrated how carbon porosity influences the double-layer (DL) capacitance,[15−17] Faradaic processes introduce additional complexity, involving mass transport of uncharged and charged species, the development of concentration gradients, and potential-dependent adsorption/release of the redox species within the pores (Figure 1).[18]

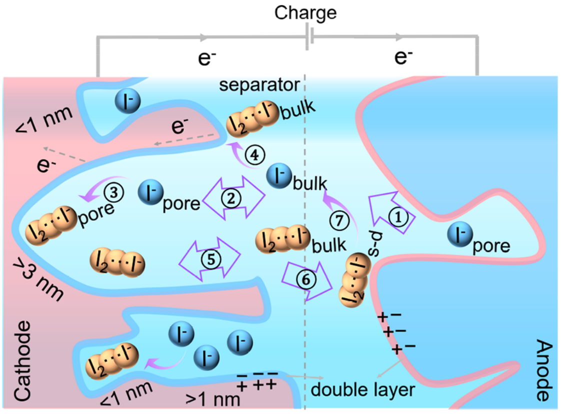

Figure 1. Illustration of charge-storage mechanism involving multiple physical transfer processes in the porous carbon electrodes and bulk solution. Iodide is used as the redox species. Self-discharge is denoted by the abbreviation "s-d".

To participate in a charge-storage process, the redox species (here I^-) must first be able to reach the carbon/electrolyte interface on the time scale of the charging step. Thus, I^- already confined within the pores of the carbon or adsorbed on the carbon surface is expected to provide Faradaic capacity on a short time scale via fast Faradaic processes (processes **3** and **4** in Figure 1). Redox species within the larger void space between the porous carbon particles must diffuse further to reach the carbon surface, and thus should respond slower. Redox species contained in the electrolyte filling the separator or the opposite carbon electrode would need to move macroscopic distances to contribute Faradaic capacity and thus would be expected to respond only on long timescales (processes **1** and **2** in Figure 1).

Because the external surface area is much smaller than the internal surface area of a porous electrode, the electrochemical reaction will primarily take place within the pores. Redox species outside of the pores (e.g., in the separator), however, may primarily react on the outer surface of the porous carbon, especially at high rates when there is insufficient time to diffuse into the pores. Concurrently, soluble species in the charged state (in this case triiodide), which are not sufficiently confined inside the pores or adsorbed on the carbon pore walls, can diffuse into the bulk electrolyte, transfer to the opposite electrode, and discharge, re-forming I^- (processes **5**−**7** in Figure 1). This self-discharge process lowers Coulombic efficiency. Thus, there is likely a trade-off between large internal surface area needed for fast electrochemical reaction as well as to adsorb/hold the charged species, and the need to provide pore volume to hold the redox electrolyte in close proximity to the carbon for high power. These expected trade-offs suggest that the pore size distribution, free volume, and internal surface area are all key properties in porous carbons for redox ECs that must be co-optimized to achieve high power density, high energy density, long cycle life and slow self discharge.

Herein we report the investigation of a range of commercial and laboratory-synthesized carbons for redox ECs. We focus on their pore-size distributions, ranging from micropore (0.6−2 nm) to mesopore (2−3 nm and 5−30 nm), specific surface area from ∼500 to ∼4000 m^2/g, and free volume in the electrode, to understand the operational mechanisms and how performance is affected by the pore structure. We then provide design guidelines for electrode engineering to maximize device performance of redox ECs. Halide ions such as iodide, the representative example used herein, undergo fast redox reactions on the surface of carbon materials. Iodide is less corrosive than bromide (when oxidized),[19,20] and thus better suited for fundamental investigation. Iodide has an ionic radius of 0.22 nm, and polyiodide has a linear structure with a length estimated to be ∼0.5 nm (I_2) to ∼0.9 nm (I_3^-).[21] Because the hydration behavior of iodide species is unknown within porous carbons and iodide is generally weakly coordinated by water, we did not further consider the hydrated ion size.[22,23] The oxidation (charging) reaction in aqueous electrolyte can be divided into two steps:[21,24] the I^- is first converted to I_2 and then complexed with the remaining I^- in the electrolyte to form water-soluble I_3^-:

$$2I^- \leftrightarrow I_2 + 2e^- \qquad E^\circ = 0.621 \text{ V vs SHE} \tag{1}$$

$$I_2 + I^- \leftrightarrow I_3^- \tag{2}$$

$$2I^- + I^- \leftrightarrow I_3^- + 2e^- \qquad E^\circ = 0.536 \text{ V vs SHE} \tag{3}$$

Porous Structures of Various Carbons. Here we consider the question, what inherent structures make a particular porous carbon a good candidate for redox ECs? For simplicity, we consider specific power, specific energy, and self-discharge rate for five different activated carbons (MSC30, MSP20, Norit, Cnovel10, and Cnovel30), which range from microporous to mesoporous (Figure 2b, Figures S1−S3). The list also includes a unique zeolite-templated carbon (ZTC), which has an atomically thin ordered framework, a well-controlled pore size[25−27] (1.2 nm as synthesized, Figure 2b) with almost no narrow micropores (<1 nm), very few larger micropores, and high specific surface area (3570 m^2/g). Due to electrical conductivity and microporosity, ZTCs have been investigated as electrode materials in supercapacitors,[28,29] hybrid capacitors,[30] and rechargeable batteries.[31,32]

Heteroatom-doped carbons have shown increased DL capacitance[33] and the ability to better capture halide anions compared to pure carbons.[34] We first excluded the existence of N or B by performing X-ray photoelectron spectroscopy (XPS) analysis (Figure S4). Trace amounts of S were detected in some mesoporous carbons (Cnovel10 and Cnovel30), which we assumed would have a negligible effect on the redox of halide anions, when comparing the porous structures.

Activated carbon particles exhibit a nonuniform morphology at the micron length scale and a broad particle-size distribution (see electron-microscopy images in Figures S5 and S6). The particles also have a range of pores with dimensions from angstroms to nanometers. In most published work, only a single parameter, such as the mean pore diameter or total

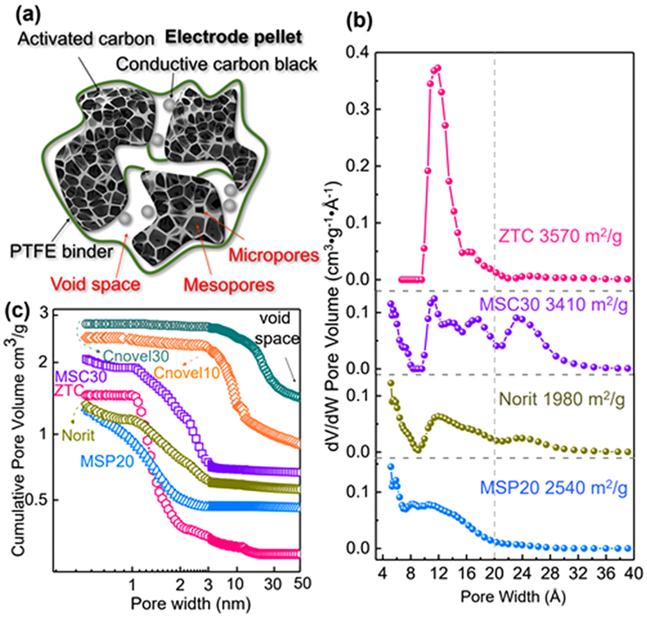

Figure 2. Structural properties of different carbons. (a) Schematic showing the porous structure of a carbon electrode on a microscopic scale, consisting of binder, conductive additive, void space between particles, mesopores, and micropores. (b) Micropore-size distributions of MSC30, Norit, MSP20, and ZTC, measured by N_2 physisorption at 77 K. The numbers labeled represent the specific BET surface area. (c) Cumulative pore-volume curves for different carbon electrodes (normalized by the dry mass of the electrode) in a combination of microspace, mesospace, and void-space volume, including Cnovel30 (dark cyan), Cnovel10 (orange), MSC30 (purple), Norit (olive), MSP20 (blue), and ZTC (pink).

surface area, is reported and used to determine structure-performance relationships. Given the multiple length scales over which diffusion, reaction, adsorption, etc. occur in a redox EC, we report a range of parameters to describe the distribution of pore sizes and free volume. Unlike ZTC, a wide distribution of pore sizes were observed in the microporous region for three different activated carbons (Figure 2b). These three activated carbons include ultranarrow micropores (<0.8 nm), which contribute substantially to the total surface area. Pores <1 nm for MSC30 and Norit contribute ~930 and ~900 m^2/g to the SSA, respectively (Table S1). MSC30 has a primary contribution from pores between 1.1 and 3 nm, Norit contains a primary contribution from micropores between 1.1 and 1.6 nm along with a small fraction from pores between 2 and 3 nm, and MSP20 has mainly pores <1.1 nm. Two mesoporous carbons, Cnovel10 and Cnovel30, have mean mesopore sizes of 5−10 nm and 20−30 nm, respectively (Figure S3).

Porous-carbon electrodes in ECs are typically composites (Figure 2a), consisting of mixtures of activated carbon, conductive additive (e.g., carbon black), and binder (e.g., PTFE) along with void space. These voids are much larger (typically micron-sized)[35] than the solvated ion. The voids contribute minimally to the total double-layer capacitance, as they provide little surface area but are likely important here for holding a reservoir of redox electrolyte that provides the Faradaic capacity. Void-space data are not normally measured or reported for redox ECs. We estimated the void space by combining helium gas pycnometry and N_2 adsorption measurements (see Note S1). The difference in void space for each electrode may arise from intrinsic parameters of the carbon materials such as skeletal structure and density. The hierarchy of pore sizes is likely important for the transport of redox species in and out of the porous carbon during charge/discharge cycles. During charging, I^- moves through void space, to mesopores, and into the micropores that hold the polyiodide charged products. Figure 2c shows a cumulative pore-volume curve for each carbon that combines the void-space data with the pore volumes determined by N_2 adsorption.

Redox Capacity and High-Rate Performance. To compare the electrochemical properties, including redox kinetics and rate capability, between various carbon electrodes, we used a three-electrode configuration with 3 M KI as the redox electrolyte and multiple separators (see details in Supporting Information, Figure S8). Uncompensated series resistance was corrected for such that each sample was charged to the same electrode potential (0.5 V vs Ag/AgCl) at various charging rates (20, 10, 5, 2, and 1 A/g) when galvanostatic charge/discharge (GCD) cycling was performed (Figure S9). The equivalent series resistance (ESR) of each electrode was determined from the *iR* potential drop between the charge and discharge steps. The cell-level capacity of a redox EC from GCD cycling includes both DL and Faradaic contributions. To investigate how the pore structure impacts the Faradaic processes, the DL contribution was subtracted. To estimate the electrode DL capacity (Note S2), voltammetry was swept at potentials where no Faradaic reactions are present (Figure S7). We found that the DL capacity was proportional to the specific surface area of the carbon (Figure 3c). However, the trend line for DL capacity did not pass through the origin (i.e., at 0 m^2/g and 0 mA·h/g). It is possible that there are other pseudocapacitive contributions due to surface species on the carbons whose contribution is independent of surface area.

After subtraction of the DL capacity, the remaining redox capacity found for each carbon correlates with the total electrode pore volume (Figure 3a) including void space (orange line). This observation shows that the void space and pore volume limit the Faradaic capacity at relevant rates (1 A/g). The mesoporous carbon, Cnovel30, had the largest pore volume and large void space and thus exhibits the highest capacity at a given rate.

The delivered redox capacity for each carbon is shown as a function of rate in Figure 3b, normalized to the capacity at 1 A/g. The normalized loss in capacity as the rate is increased provides a measure of the ease of redox-couple transport in the porous carbon. The normalized-capacity loss with increasing rate decreased in the order of MSP20 > Cnovel10 ≈ Cnovel30 > Norit > MSC30 > ZTC. Among the three activated carbons, the trend in normalized capacity loss correlates with the pore sizes (Figure 2b). ZTC, with a micropore size of 1.2 nm, exhibits the least capacity loss at high rates, while MSP20, with the smallest pore sizes, exhibits the most. Micropores larger than 1 nm appear important for fast-rate capability. Even though both MSC30 and Norit contain pores larger than ZTC, they also contain substantial ultra-narrow pores (<0.8 nm), which likely lead to the inferior rate capability compared to ZTC with well-controlled 1.2 nm pores. Cnovel10 and Cnovel30 have larger mesopore volumes and void spaces, therefore requiring longer diffusion pathways for redox species, explaining the large loss of normalized capacity for these carbons at high rates compared to ZTC or MSC30. Although

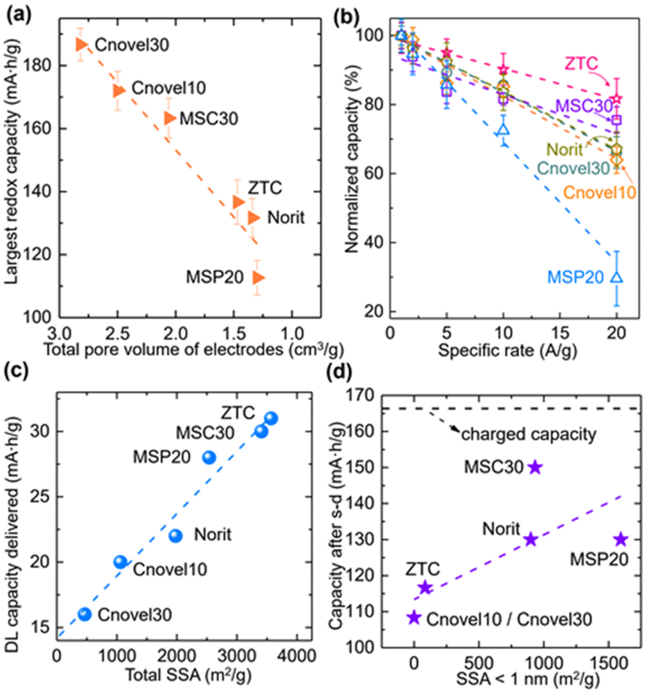

Figure 3. Correlation between pore properties and electrochemical response. (a) Total pore volume of different carbons as electrodes and corresponding specific redox capacity (double-layer capacity contribution subtracted) delivered at 1 A/g. (b) Rate-dependent capacity of porous carbons as positive electrodes cycled (in order) at 20, 10, 5, and 2 A/g, normalized to capacity at 1 A/g. (c) Total specific surface area for different carbons and corresponding double-layer capacity. (d) Specific surface area contributed from pores ≤1 nm for different carbons and discharge capacity retained after the self-discharge test. All electrode masses were normalized to the dry mass of the positive electrode.

Cnovel30 and Convel10 deliver the largest redox capacity at slow rates due to the largest electrode pore volume, the capacities exhibited by microporous carbons MSC30 and ZTC are superior at 20 A/g (Figure S10).

An interesting comparison is between the MSP20 and Norit carbon. MSP20 has a larger surface area (2540 m^2/g) than Norit (1980 m^2/g), but MSP20 has lower capacity and the largest performance loss as the rate increases. This behavior is likely explained by the fact that MSP20 has primarily pores less than 1 nm in diameter. The small pores may retard iodide species diffusion inside the pores at high rate. The redox capacity at 20 A/g for MSP20 is almost 4 times less than that for MSC30 and Cnovel30 (Figure S10). Norit carbon, which contains micropores larger than 1.1 nm that contribute to ~55% of the surface area (Table S1), provides improved mass transport of the redox species compared to MSP20. This finding shows that high surface area alone is insufficient for designing carbons in redox ECs and suggests that hierarchical pore structures are critical.

Self-Discharge. The carbon-pore structure also substantially influenced the rate of self-discharge. Self-discharge was quantified by measuring the capacity retention after holding a cell charged at 1 A/g for 6 h at open circuit, compared to when it was first charged (at 1 mA·h, Figure 3d). The cell with MSC30 retained ~90% of its capacity, while those with mesoporous carbons, Cnovel10 or Cnovel30, retained only ~65% of the capacity. This result indicates faster self-discharge due to diffusion of the charged redox species from positive to negative electrode for the mesoporous carbons. Further, while ZTC outperformed the Norit and MSP20 carbons with respect to capacity, it exhibited worse self-discharge with only 70% capacity retention after 6 h at open circuit. As ZTC possesses the highest surface area of the carbon materials investigated, it is clear several other factors are important to retard cross diffusion. ZTC has a narrow pore-size distribution centered at 1.2 nm. These pores appear to be slightly too large to effectively confine the charged products and prevent self-discharge. Figure 3d and Table S1 show that the surface area provided by pores smaller than 1 nm appear important to inhibit self-discharge by containing and trapping charged triiodide species. The three microporous carbons, MSC30, Norit, and MSP20, all contain a substantial fraction of pores <1 nm, yielding a slower self-discharge rate than the carbons without these <1 nm pores (Cnovel10, Cnovel30, and ZTC).

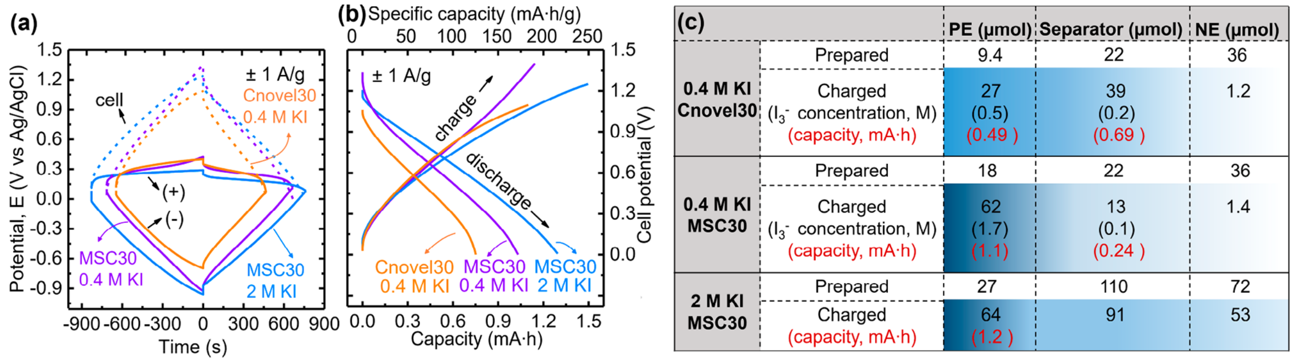

(c)		PE (μmol)	Separator (μmol)	NE (μmol)
0.4 M KI Cnovel30	Prepared	9.4	22	36
	Charged (I_3^- concentration, M) (capacity, mA·h)	27 (0.5) (0.49)	39 (0.2) (0.69)	1.2
0.4 M KI MSC30	Prepared	18	22	36
	Charged (I_3^- concentration, M) (capacity, mA·h)	62 (1.7) (1.1)	13 (0.1) (0.24)	1.4
2 M KI MSC30	Prepared	27	110	72
	Charged (capacity, mA·h)	64 (1.2)	91	53

Figure 4. Quantification of redox-species distribution in the cell and relation to performance. (a) Galvanostatic charge/discharge profiles for the positive, negative, and total three-electrode cell cycled at 1 A/g (normalized to the mass of the positive electrode only). The cells were assembled with two different activated carbons (MSC30 and Cnovel30) as positive electrodes and different concentrations of KI as redox electrolyte: 0.4 M KI with Cnovel30 (orange), 0.4 M KI with MSC30 (purple), and 2 M KI with MSC30 (blue), respectively. (b) Galvanostatic charge−discharge (GCD) profiles for two-electrode cells. (c) Table showing the quantity of iodide in the positive electrode (PE), separator, and negative electrode (NE) for as-prepared and charged cells. The concentration numbers are estimated on the basis of the total amount of iodine species found by elemental analysis in the charged cell component and capacity numbers represent the estimated redox capacity contribution from the same iodine species. For details, see Note S3.

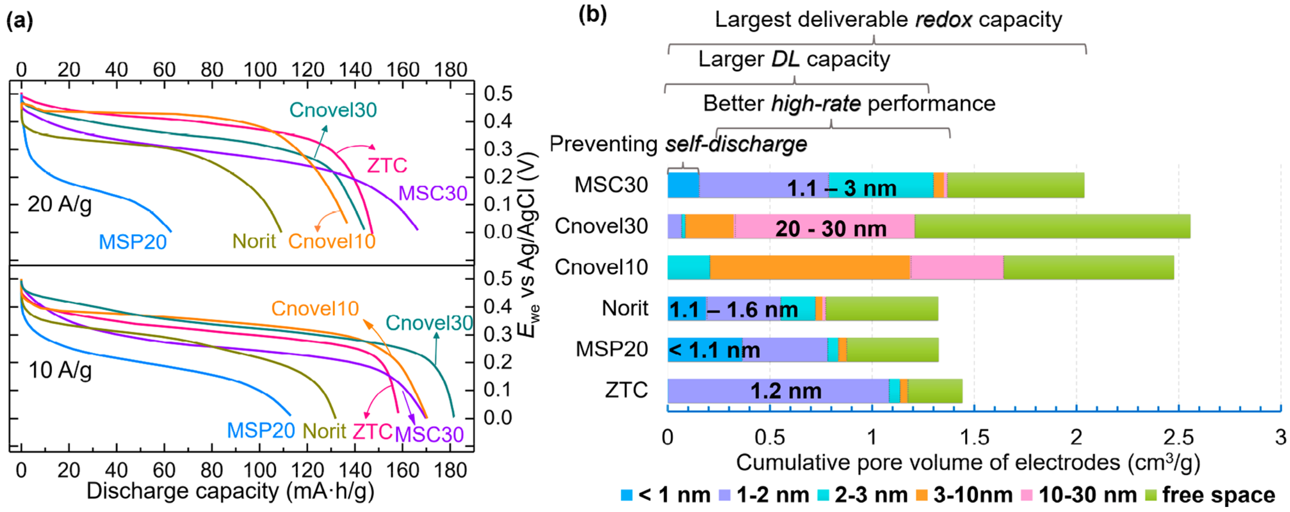

Figure 5. Design principles for porous carbon electrodes. (a) Discharge curves of different carbons as positive electrodes at high rates (20 and 10 A/g, normalized to the dry mass of positive electrode) showing overall capacity (redox plus DL contribution). (b) Pore volume contributed from various pore size regions for different carbons as electrodes (normalized to the mass of electrodes).

The retention behavior of ultranarrow micropores have been observed previously for polyiodide[14] and polysulfide.[36]

Quantification of Redox Species Location. Asymmetric cells were designed and built with aqueous KI (0.4 and 2 M) as the electrolyte to quantitatively analyze the distribution and redistribution of the redox species during charge and discharge process (see the Supporting Information for details). A two-electrode configuration was used with an oversized negative electrode (5 times larger in mass than the positive electrode) on which charge storage was only via DL formation. Two very different porous carbons were chosen as positive electrodes: one microporous carbon, MSC30, with a SSA of ~3410 m^2/g and pore sizes between 1.1 and 3 nm and the other, a mesoporous carbon, Cnovel30, with a lower surface area of ~470 m^2 /g but with a much larger average pore size of 20−30 nm.

The assembled cells were filled with 0.4 M KI as an electrolyte and cycled at the rate of 1 A/g to 1.1 mA·h (Figure 4a and b). The low KI concentration was chosen to achieve total consumption of the iodide, which is evidenced by electrochemical behavior that transitions from redox-like (i.e., potential is relatively flat with charge) to capacitive (where potential changes linearly with charge at longer times). We then measured how the charged species redistribute during the subsequent discharge process. A glass-fiber (GF) separator was inserted to prevent direct electrical contact between the electrodes, but no ion-selective membrane was used and the dissolved iodide/triiodide could freely transfer through the cell (i.e., between the positive and negative electrode). Subsequently, the electrodes and GF separator for an as-prepared and fully charged cell were dissolved individually. The dissolution of the carbon electrode material was difficult as it is not soluble in common acids. Graphitic carbon is often burned in a furnace and the resulting ash is dissolved for analysis. However, such a dry-ashing approach would lead to a loss of the volatile iodine species. We dissolved the electrodes in a mixture of heated perchloric acid and nitric acid (Figure S11).[37] Inductively coupled-plasma atomic-emission spectrometry (ICP-AES) was used to measure the iodine content in the dissolved components (Figure 4c).

In both cells, Cnovel30 with 0.4 M KI and MSC30 with 0.4 M KI, the iodide that was originally adsorbed onto the negative electrode was nearly completely removed after charging (only ~3% left, Figure 4c). Cnovel30 confines substantially less triiodide (27 μmol, 4.5 mmol/g) within the positive electrode than MSC30 (62 μmol, 10.3 mmol/g) when charged in the 0.4 M KI solution and exhibits a smaller polyiodide concentration difference between the positive electrode and separator (~0.3 M) than MSC30 (~1.6 M) in the charged state. The Cnovel30 cell also delivered less capacity (0.75 mA·h, 125 mA·h/g) than MSC30 (1.03 mA·h, 172 mA·h/g), even if both were equally charged (1.1 mA·h, 183 mA·h/g) (Figure 4b). These results are consistent with fast self-discharge for the carbons with large pores that cannot effectively confine and adsorb the polyiodides formed.

We next studied a higher concentration electrolyte (2 M KI) and found that the iodide is not depleted over the whole cell during charging. Interestingly, with MSC30 as the working electrode, substantially higher capacity (1.3 mA·h, 217 mA·h/g) relative to 0.4 M KI (1.03 mA·h, 172 mA·h/g; Figure 4b) was not found. A decrease in Coulombic efficiency, however, from 91% for 0.4 M KI to 86% for 2 M KI was observed in one ~30 min GCD cycle. Correlating the fact (Figure 4c) that the carbon was not able to confine significantly more iodide for 2 M KI (64 μmol) than for 0.4 M KI (62 μmol), the extra charged triiodide diffused into the "bulk" solution, contributing to self-discharge. Hence, we conclude that it is rather the quantity of active species that a carbon electrode can confine in the charged state that is important for capacity, instead of only the overall amount of redox species in the electrolyte. This finding also emphasizes the importance of choosing the appropriate hierarchically porous carbon.

Design Principles. The overall rate performance of a redox EC is governed by both the Faradaic and DL capacity, with the DL component increasing in importance at high rate. MSC30 yielded the highest capacity of all carbons at a rate of 20 A/g (Figure 5a), while maintaining excellent self-discharge performance. At 10 A/g, MSC30 provided the second highest capacity. Choosing the appropriate carbon is clearly critical for redox EC technology. For example, comparing MSP20 and MSC30, the latter provides a 4 times more redox capacity (and

3 times overall capacity improvement) at a rate of 20 A/g, while decreasing self-discharge (capacity retention of >90%, versus <80% after 6 h). These dramatic differences were unexpected when simply comparing the SSA (3410 m^2/g versus 2540 m^2/g).

We next compare MSP20 and ZTC to illustrate the general features of redox-EC carbon design principles. MSP20, with primary pores <1.1 nm, yielded the worst redox-rate performance (which we conclude is due to mass-transport limitations in the small pores) but has slow self-discharge. ZTC, which has a larger more-uniform pore size of 1.2 nm, delivered better redox performance, but with worse self-discharge. Therefore, we propose that, when halides are utilized as redox species, a superior carbon electrode should have (Figure 5b) (i) pores smaller than 1 nm, which are essential for effectively preventing self-discharge and contribute DL capacity that is increasingly important at high rates; (ii) micropores larger than ∼1 nm to provide pathways for electrolyte transport and correspondingly better high-rate capability for Faradaic processes; and (iii) a large pore volume contributed by meso/micropores of the carbon, with the addition of void space, which provides a reservoir of electrolyte in close proximity to the porous carbon to achieve a high redox capacity. These design criteria reveal activated carbons like MSC30, with multiple pore structures containing ultranarrow pores of <0.8 nm (for slow self-discharge) and larger pores of 1.1−3 nm (for high-rate capability), as well as a modest contribution of void space in the electrode, provide the highest performance. Better engineering of the void space would likely lead to further improvements.

In summary, we related the pore structure of a variety of porous carbon materials to operating mechanisms and performance when applied as electrodes in redox-enhanced capacitors. This work provides a fundamental analysis of how to identify carbons with the best performance and optimize a specific carbon for redox ECs. Although MSC30 appears promising, the absolute pore sizes forming the basis for this analysis are unlikely universal for all redox species, considering that the intrinsic ion size of each species influences the interactions within nanoporous confinement. Therefore, the experimental protocols and results herein should serve as guidelines that, when also combined with knowledge of the size of the redox species and its solubility and interaction with carbon, enable the rational design of carbon electrodes for redox ECs.

■ ASSOCIATED CONTENT

Supporting Information

The Supporting Information is available free of charge at https://pubs.acs.org/doi/10.1021/acsenergylett.0c02424.

> Experimental details; fabrication of redox-enhanced electrochemical capacitors; assembly of two- and three-electrode cells; digestion of carbon electrodes and separators; electrochemical measurements including the galvanostatic charge/discharge curves and CV curves; calculation of void-space volume in carbon electrodes; estimation of redox capacity contribution and polyiodide concentration from the amount of consumed iodide; N_2 adsorption isotherms, partial and accumulated surface area, pore-size distribution, XPS measurements, SEM and TEM images of carbon materials (PDF)

■ AUTHOR INFORMATION

Corresponding Authors

Jian-Feng Li − *State Key Laboratory of Physical Chemistry of Solid Surfaces, Collaborative Innovation Center of Chemistry for Energy Materials (iChEM), College of Chemistry and Chemical Engineering, Xiamen University, Xiamen 361005, P. R. China;* orcid.org/0000-0003-1598-6856; Email: li@xmu.edu.cn

Seung Joon Yoo − *School of Materials Science and Engineering, Gwangju Institute of Science and Technology, Gwangju 61005, Republic of Korea*; Email: sjoonyoo@gist.ac.kr

Shannon W. Boettcher − *Department of Chemistry and Biochemistry, The Materials Science Institute, and the Oregon Center for Electrochemistry, University of Oregon, Eugene, Oregon 97403, United States;* orcid.org/0000-0001-8971-9123; Email: swb@uoregon.edu

Authors

Yang Zhao − *State Key Laboratory of Physical Chemistry of Solid Surfaces, Collaborative Innovation Center of Chemistry for Energy Materials (iChEM), College of Chemistry and Chemical Engineering, Xiamen University, Xiamen 361005, P. R. China; Department of Chemistry and Biochemistry, University of California Santa Barbara, Santa Barbara, California 93106, United States*

Erin E. Taylor − *Department of Chemistry & Biochemistry, Montana State University, Bozeman, Montana 59717, United States;* orcid.org/0000-0002-2202-1131

Xudong Hu − *Department of Chemistry and Biochemistry, University of California Santa Barbara, Santa Barbara, California 93106, United States*

Brian Evanko − *Materials Department, University of California Santa Barbara, Santa Barbara, California 93106, United States*

Xiaojun Zeng − *Department of Chemistry and Biochemistry, University of California Santa Barbara, Santa Barbara, California 93106, United States*

Hengbin Wang − *Mitsubishi Chemical Center for Advanced Materials, University of California, Santa Barbara, Santa Barbara, California 93106, United States*

Ryohji Ohnishi − *Science & Innovation Center, Mitsubishi Chemical Corporation, Yokohama 227-8502, Japan*

Takaki Tsukazaki − *R&D Center, Kansai Coke and Chemicals Co., Ltd, Amagasaki 660-0095, Japan*

Nicholas P. Stadie − *Department of Chemistry & Biochemistry, Montana State University, Bozeman, Montana 59717, United States;* orcid.org/0000-0002-1139-7846

Galen D. Stucky − *Department of Chemistry and Biochemistry, University of California Santa Barbara, Santa Barbara, California 93106, United States; Materials Department, University of California Santa Barbara, Santa Barbara, California 93106, United States;* orcid.org/0000-0002-0837-5961

Complete contact information is available at: https://pubs.acs.org/10.1021/acsenergylett.0c02424

Notes

The authors declare no competing financial interest.

■ ACKNOWLEDGMENTS

This work was supported by the Mitsubishi Chemical Center for Advanced Materials. The MRL Shared Experimental Facilities are supported by the MRSEC Program of the NSF under Award No. DMR 1720256; a member of the NSF-funded Materials Research Facilities Network (www.mrfn.org). This work was supported by the National Research Foundation of Korea (NRF) grant funded by the Korea government (MSIT) (No. 2020R1F1A1072086). The work at Xiamen University was supported by the National Science Foundation of China through grant number 21522508. Y.Z. acknowledges financial support from the China Scholarship Council (No. 201706310206). S.W.B. acknowledges funding from the NSF under award number CHE-1955106.

■ REFERENCES

(1) Roldán, S.; Blanco, C.; Granda, M.; Menéndez, R.; Santamaría, R. Towards a Further Generation of High-Energy Carbon-Based Capacitors by Using Redox-Active Electrolytes. *Angew. Chem., Int. Ed.* **2011**, *50* (7), 1699−1701.

(2) Senthilkumar, S. T.; Selvan, R. K.; Melo, J. S. Redox Additive/Active Electrolytes: A Novel Approach to Enhance the Performance of Supercapacitors. *J. Mater. Chem. A* **2013**, *1* (40), 12386−12394.

(3) Fic, K.; Meller, M.; Frackowiak, E. Interfacial Redox Phenomena for Enhanced Aqueous Supercapacitors. *J. Electrochem. Soc.* **2015**, *162* (5), A5140−A5147.

(4) Evanko, B.; Boettcher, S. W.; Yoo, S. J.; Stucky, G. D. Redox-Enhanced Electrochemical Capacitors: Status, Opportunity, and Best Practices for Performance Evaluation. *ACS Energy Lett.* **2017**, *2* (11), 2581−2590.

(5) Lee, J.; Srimuk, P.; Fleischmann, S.; Su, X.; Hatton, T. A.; Presser, V. Redox-Electrolytes for Non-Flow Electrochemical Energy Storage: A Critical Review and Best Practice. *Prog. Mater. Sci.* **2019**, *101*, 46−89.

(6) Chen, L.; Bai, H.; Huang, Z.; Li, L. Mechanism Investigation and Suppression of Self-Discharge in Active Electrolyte Enhanced Supercapacitors. *Energy Environ. Sci.* **2014**, *7* (5), 1750−1759.

(7) Chun, S.-E.; Evanko, B.; Wang, X.; Vonlanthen, D.; Ji, X.; Stucky, G. D.; Boettcher, S. W. Design of Aqueous Redox-Enhanced Electrochemical Capacitors with High Specific Energies and Slow Self-Discharge. *Nat. Commun.* **2015**, *6* (1), 7818.

(8) Yoo, S. J.; Evanko, B.; Wang, X.; Romelczyk, M.; Taylor, A.; Ji, X.; Boettcher, S. W.; Stucky, G. D. Fundamentally Addressing Bromine Storage through Reversible Solid-State Confinement in Porous Carbon Electrodes: Design of a High-Performance Dual-Redox Electrochemical Capacitor. *J. Am. Chem. Soc.* **2017**, *139* (29), 9985−9993.

(9) Evanko, B.; Yoo, S. J.; Chun, S.-E.; Wang, X.; Ji, X.; Boettcher, S. W.; Stucky, G. D. Efficient Charge Storage in Dual-Redox Electrochemical Capacitors through Reversible Counterion-Induced Solid Complexation. *J. Am. Chem. Soc.* **2016**, *138* (30), 9373−9376.

(10) Lee, J.; Krüner, B.; Tolosa, A.; Sathyamoorthi, S.; Kim, D.; Choudhury, S.; Seo, K.-H.; Presser, V. Tin/Vanadium Redox Electrolyte for Battery-Like Energy Storage Capacity Combined with Supercapacitor-Like Power Handling. *Energy Environ. Sci.* **2016**, *9* (11), 3392−3398.

(11) Hu, L.; Shi, C.; Guo, K.; Zhai, T.; Li, H.; Wang, Y. Electrochemical Double-Layer Capacitor Energized by Adding an Ambipolar Organic Redox Radical into the Electrolyte. *Angew. Chem., Int. Ed.* **2018**, *57* (27), 8214−8218.

(12) Lota, G.; Frackowiak, E. Striking Capacitance of Carbon/Iodide Interface. *Electrochem. Commun.* **2009**, *11* (1), 87−90.

(13) Senthilkumar, S. T.; Selvan, R. K.; Lee, Y. S.; Melo, J. S. Electric Double Layer Capacitor and Its Improved Specific Capacitance Using Redox Additive Electrolyte. *J. Mater. Chem. A* **2013**, *1* (4), 1086−1095.

(14) Lee, J.; Srimuk, P.; Fleischmann, S.; Ridder, A.; Zeiger, M.; Presser, V. Nanoconfinement of Redox Reactions Enables Rapid Zinc Iodide Energy Storage with High Efficiency. *J. Mater. Chem. A* **2017**, *5* (24), 12520−12527.

(15) Chmiola, J.; Yushin, G.; Gogotsi, Y.; Portet, C.; Simon, P.; Taberna, P. L. Anomalous Increase in Carbon Capacitance at Pore Sizes Less Than 1 Nanometer. *Science* **2006**, *313* (5794), 1760.

(16) Largeot, C.; Portet, C.; Chmiola, J.; Taberna, P.-L.; Gogotsi, Y.; Simon, P. Relation between the Ion Size and Pore Size for an Electric Double-Layer Capacitor. *J. Am. Chem. Soc.* **2008**, *130* (9), 2730−2731.

(17) Zhang, L.; Yang, X.; Zhang, F.; Long, G.; Zhang, T.; Leng, K.; Zhang, Y.; Huang, Y.; Ma, Y.; et al. Controlling the Effective Surface Area and Pore Size Distribution of sp^2 Carbon Materials and Their Impact on the Capacitance Performance of These Materials. *J. Am. Chem. Soc.* **2013**, *135* (15), 5921−5929.

(18) Akinwolemiwa, B.; Peng, C.; Chen, G. Z. Redox Electrolytes in Supercapacitors. *J. Electrochem. Soc.* **2015**, *162* (5), A5054−A5059.

(19) Xie, C.; Zhang, H.; Xu, W.; Wang, W.; Li, X. A Long Cycle Life, Self-Healing Zinc−Iodine Flow Battery with High Power Density. *Angew. Chem., Int. Ed.* **2018**, *57* (35), 11171−11176.

(20) Evanko, B.; Yoo, S. J.; Lipton, J.; Chun, S.-E.; Moskovits, M.; Ji, X.; Boettcher, S. W.; Stucky, G. D. Stackable Bipolar Pouch Cells with Corrosion-Resistant Current Collectors Enable High-Power Aqueous Electrochemical Energy Storage. *Energy Environ. Sci.* **2018**, *11* (10), 2865−2875.

(21) Weng, G.-M.; Li, Z.; Cong, G.; Zhou, Y.; Lu, Y.-C. Unlocking the Capacity of Iodide for High-Energy-Density Zinc/Polyiodide and Lithium/Polyiodide Redox Flow Batteries. *Energy Environ. Sci.* **2017**, *10* (3), 735−741.

(22) Ohkubo, T.; Konishi, T.; Hattori, Y.; Kanoh, H.; Fujikawa, T.; Kaneko, K. Restricted Hydration Structures of Rb and Br Ions Confined in Slit-Shaped Carbon Nanospace. *J. Am. Chem. Soc.* **2002**, *124* (40), 11860−11861.

(23) Levi, M. D.; Sigalov, S.; Salitra, G.; Elazari, R.; Aurbach, D. Assessing the Solvation Numbers of Electrolytic Ions Confined in Carbon Nanopores under Dynamic Charging Conditions. *J. Phys. Chem. Lett.* **2011**, *2* (2), 120−124.

(24) Boschloo, G.; Hagfeldt, A. Characteristics of the Iodide/Triiodide Redox Mediator in Dye-Sensitized Solar Cells. *Acc. Chem. Res.* **2009**, *42* (11), 1819−1826.

(25) Nishihara, H.; Kyotani, T. Zeolite-Templated Carbons − Three-Dimensional Microporous Graphene Frameworks. *Chem. Commun.* **2018**, *54* (45), 5648−5673.

(26) Taylor, E. E.; Garman, K.; Stadie, N. P. Atomistic Structures of Zeolite-Templated Carbon. *Chem. Mater.* **2020**, *32* (7), 2742−2752.

(27) Nishihara, H.; Fujimoto, H.; Itoi, H.; Nomura, K.; Tanaka, H.; Miyahara, M. T.; Bonnaud, P. A.; Miura, R.; Suzuki, A.; et al. Graphene-Based Ordered Framework with a Diverse Range of Carbon Polygons Formed in Zeolite Nanochannels. *Carbon* **2018**, *129*, 854−862.

(28) Kajdos, A.; Kvit, A.; Jones, F.; Jagiello, J.; Yushin, G. Tailoring the Pore Alignment for Rapid Ion Transport in Microporous Carbons. *J. Am. Chem. Soc.* **2010**, *132* (10), 3252−3253.

(29) Itoi, H.; Nishihara, H.; Kogure, T.; Kyotani, T. Three-Dimensionally Arrayed and Mutually Connected 1.2-nm Nanopores for High-Performance Electric Double Layer Capacitor. *J. Am. Chem. Soc.* **2011**, *133* (5), 1165−1167.

(30) Dubey, R. J. C.; Colijn, T.; Aebli, M.; Hanson, E. E.; Widmer, R.; Kravchyk, K. V.; Kovalenko, M. V.; Stadie, N. P. Zeolite-Templated Carbon as a Stable, High Power Magnesium-Ion Cathode Material. *ACS Appl. Mater. Interfaces* **2019**, *11* (43), 39902−39909.

(31) Stadie, N. P.; Wang, S.; Kravchyk, K. V.; Kovalenko, M. V. Zeolite-Templated Carbon as an Ordered Microporous Electrode for Aluminum Batteries. *ACS Nano* **2017**, *11* (2), 1911−1919.

(32) Dubey, R. J. C.; Nüssli, J.; Piveteau, L.; Kravchyk, K. V.; Rossell, M. D.; Campanini, M.; Erni, R.; Kovalenko, M. V.; Stadie, N. P. Zeolite-Templated Carbon as the Cathode for a High Energy

Density Dual-Ion Battery. *ACS Appl. Mater. Interfaces* **2019**, *11* (19), 17686−17696.

(33) Guo, H.; Gao, Q. Boron and Nitrogen Co-Doped Porous Carbon and Its Enhanced Properties as Supercapacitor. *J. Power Sources* **2009**, *186* (2), 551−556.

(34) Lee, J.-H.; Byun, Y.; Jeong, G. H.; Choi, C.; Kwen, J.; Kim, R.; Kim, I. H.; Kim, S. O.; Kim, H.-T. High-Energy Efficiency Membraneless Flowless Zn−Br Battery: Utilizing the Electrochemical−Chemical Growth of Polybromides. *Adv. Mater.* **2019**, *31* (52), 1904524.

(35) Hwang, J. Y.; Li, M.; El-Kady, M. F.; Kaner, R. B. Next-Generation Activated Carbon Supercapacitors: A Simple Step in Electrode Processing Leads to Remarkable Gains in Energy Density. *Adv. Funct. Mater.* **2017**, *27* (15), 1605745.

(36) Hippauf, F.; Nickel, W.; Hao, G.-P.; Schwedtmann, K.; Giebeler, L.; Oswald, S.; Borchardt, L.; Doerfler, S.; Weigand, J. J.; Kaskel, S. The Importance of Pore Size and Surface Polarity for Polysulfide Adsorption in Lithium Sulfur Batteries. *Adv. Mater. Interfaces* **2016**, *3* (18), 1600508.

(37) Buzzelli, G.; Mosen, A. W. Perchloric Acid Dissolution of Graphite and Pyrolytic Carbon. *Talanta* **1977**, *24* (6), 383−385.